PAGaN II: The Evolution of AGN Jets on Sub-Parsec Scales[†]

Junghwan Oh[1], Sascha Trippe[1], Sincheol Kang[2,3], Jae-Young Kim[1,4], Jong-Ho Park[1], Taeseok Lee[1],
Daewon Kim[1], Motoki Kino[3], Sang-Sung Lee[3], and Bong Won Sohn[3]

[1]Department of Physics and Astronomy, Seoul National University, Gwanak-gu, Seoul 08826, Korea
joh@astro.snu.ac.kr, trippe@astro.snu.ac.kr
[2]University of Science and Technology, Yuseong-gu, Daejeon 34113, Korea
[3]Korea Astronomy and Space Science Institute, Yuseong-gu, Daejeon 34055, Korea
[4]Max-Planck Institut für Radioastronomie, Auf dem Hügel 69, D-53121 Bonn, Germany

Abstract: We report first results from KVN and VERA Array (KaVA) VLBI observations obtained in the frame of our *P*lasma-physics of *A*ctive *Ga*lactic *N*uclei (PAGaN) project. We observed eight selected AGN at 22 and 43 GHz in single polarization (LCP) between March 2014 and April 2015. Each source was observed for 6 to 8 hours per observing run to maximize the uv coverage. We obtained a total of 15 deep high-resolution images permitting the identification of individual circular Gaussian jet components and three spectral index maps of BL Lac, 3C 111 and 3C 345 from simultaneous dual-frequency observations. The spectral index maps show trends in agreement with general expectations – flat core and steep jets – while the actual value of the spectral index for jets shows indications for a dependence on AGN type. We analyzed the kinematics of jet components of BL Lac and 3C 111, detecting superluminal proper motions with maximum apparent speeds of about $5c$. This constrains the lower limits of the intrinsic component velocities to ∼ $0.98c$ and the upper limits of the angle between jet and line of sight to ∼20°. In agreement with global jet expansion, jet components show systematically larger diameters d at larger core distances r, following the global relation $d \approx 0.2r$, albeit within substantial scatter.

Key words: galaxies: active, jets — radio continuum: galaxies — techniques: interferometric

1. Introduction

Active Galactic Nuclei (AGN) are the most powerful persistent sources of energy in the universe. It is widely accepted that their large powers, sometimes reaching up to 10^{15} $L_{\odot}$, are provided by accretion of interstellar matter onto supermassive black holes (e.g., Ferrarese & Ford 2005; Beckmann & Shrader 2012). Such an extreme environment provides a natural laboratory for the study a variety of high-energy physical processes. Especially at radio frequencies, AGN tend to show strong jet outflows extending out to Megaparsec scales emitting synchrotron continuum radiation. Images from Very Long Baseline Interferometry (VLBI) studies (e.g., Lister et al. 2009a,b) have revealed that jets are highly collimated and occasionally show extreme kinematics leading to apparent superluminal proper motions of jet components. Despite of decade-long research efforts, there is no established mechanism providing a full explanation for the formation and launching of jets. Although already Blandford & Znajek (1977) provided a theoretical model which explains the formation of jets via the interplay of accreted matter, black hole rotation, and magnetic fields in accretion disks, the details are insufficiently understood as yet.

The internal plasma-physical conditions of jets find expression in (1) their spatial structure and kinematics, (2) characteristic variations of optical depth, and (3) the strength and orientation of magnetic field. Apparent superluminal proper motions of jets can be detected by tracking bright "knots" (i.e., individual, well-separated components) moving away from an optically thick core. For assessing the structure and kinematics of jets, high resolution mapping is essential to distinguish and track the discrete knots. Furthermore, the observation should be conducted at two (or more) frequencies simultaneously in order to obtain a spectral index map of the source, which in turn provides information on optical depths of core and jets. Furthermore, polarimetric observations, if available, unveil the geometries and strengths of magnetic fields.

The KVN and VERA Array (KaVA), the combination of the Korean VLBI Network (KVN) and the Japanese VLBI Exploration of Radio Astrometry (VERA) radio arrays, is ideal for such studies. KVN, a recently built array with three 21-meter antennas, has unique properties such as four-channel dual-polarization receivers operating simultaneously at frequencies of 22, 43, 86 and 129 GHz (Lee et al. 2014). The small number of baselines, however, limits its imaging capability as well as relatively short (up to 500 km) baseline length. On the other hand, VERA has characteristics that are complementary to those of KVN in many ways. It has longer baselines (up to 2300 km) and four antennas but lacks shorter baselines. The

Table 1
PAGaN observations with KaVA in 2014 and 2015

Year	Date	Source	Frequency (GHz)	Obs. time (hrs)
2014	Apr. 17	BL LAC	43	6
2014	Mar. 15	3C111	43	6
2014	Oct. 22	BL LAC	22	7
2014	Oct. 22	1624+690	22	7
2014	Oct. 23	3C111	22	8
2014	Nov. 3	1055+018	22	6
2014	Nov. 3	3C84	22	6
2014	Nov. 4	0133+476	22	6
2014	Nov. 5	3C120	22	6
2015[a]	Mar. 31	3C345	22	7.5
2015	Apr. 1	3C345	43	7.5
2015[a]	Mar. 31	BL LAC	22	8
2015	Apr. 1	BL LAC	43	8
2015[a]	Apr. 1	3C111	22	7.5
2015	Apr. 2	3C111	43	7.5

[a] Data from VERA station Iriki not available.

joint array, KaVA, employs a total of seven antennas at frequencies of 22 and 43 GHz, resulting in angular resolutions of 1.2 and 0.6 mas, respectively. Although simultaneous multi-frequency observation is not possible, this limit can be overcome by observing targets consecutively at both frequencies. The imaging capability of KaVA has been discussed in detail by Niinuma et al. (2014).

Motivated by the arguments given above, we commenced the *P*lasma-physics of *A*ctive *Ga*lactic *N*uclei (PAGaN) project which studies the plasma-physical properties of AGN jets via dedicated multi-frequency and polarimetric (where possible) VLBI observations. In the present paper (PAGaN II), we present and discuss our first results from KaVA mapping observations. In a companion paper (PAGaN I, Kim et al. 2015), we present first results from polarimetric observations with KVN.

2. Observations and Data Reduction

We initially selected seven radio-bright AGN with extended structure on milliarcsecond scales: 1055+018, 0133+476, 1642+690, 3C 120, 3C 84, 3C 111, and BL Lacertae (BL Lac). In 2015, we excluded sources with relatively high redshift (1055+018, 0133+476, and 1642+690) because the fine structure of their jets was not obvious at the relatively coarse angular scales. We also replaced 3C 84 by 3C 345, since observation data for 3C 84 can be obtained from other observations that are using 3C 84 as a calibrator. Accordingly, the total number of targets observed at least once is eight.

As summarized in Table 1, our KaVA observations cover three seasons (spring 2014, fall 2014, spring 2015). Between two and seven sessions were carried out in each season. In 2014, 43 GHz and 22 GHz data were obtained separately in spring and fall, respectively. In

spring 2015, 22 and 43 GHz observations for any given source were conducted within two consecutive days. In order to obtain good *uv* coverage, all observations covered substantial fractions of full tracks, each consisting of multiple 10-minute scans on source. Each source was observed for 6–8 hours in 2014 and 7.5–8 hours in 2015. Single-polarization (left-handed circular, LHC) light was recorded at a rate of 1 Gbps, resulting in a bandwidth of 256 MHz. The observation mode was C5, which provides 16 intermediate frequencies (IF) and 128 channels in each IF. All seven antennas in KaVA were used except for the 22-GHz observation in 2015 when data from VERA Iriki were lost for an unknown reason after correlation. The correlation was performed in the Korea-Japan Correlation Center (KJCC) in Daejeon (Yeom et al. 2009; Lee et al. 2015).

We calibrated the correlated data using the NRAO Astronomical Image Processing System (AIPS) software package. At the beginning, we clipped channels 1–12 and 116–128 (out of 128 in total) from each IF to avoid known band-edge effects. In AIPS, we performed a-priori amplitude calibration with the task `APCAL`. This task uses the opacity-corrected system temperature (T_{sys}^*) and gain curve of each antenna which are measured during the observations. Next, we ran the task `FRING` for fringe fitting. After calibration, we imaged our data with the Caltech Difmap software package. We deconvolved our maps with `CLEAN` and applied phase self-calibration repeatedly, and then applied amplitude self-calibration starting with long (10^6 minutes) time interval to shorter time range. Once `CLEAN`ed maps were made, we fitted sets of circular Gaussian model components to the maps using the DIFMAP function `modelfit`. We determined component locations with point-like models and then iterated `modelfit` 3–5 times to fit their sizes and fluxes (Jorstad et al. 2005). For each model component, we extracted S_{tot} (total flux), S_{peak} (peak intensity), r (radial distance from the core), θ (the position angle of the component measured from north to east), and d (size), with the uncertainties of the parameters calculated according to Lee et al. (2008).

3. Results

In total eight sources were observed for at least one epoch each. Four targets were observed only at 22 GHz. Data for two sources – 3C 111 and BL Lac – were obtained for all epochs and all frequencies. Observational results for all sources are listed in Table 2. In the following, naturally weighted [`uvweight (0,−1)`] images of each source are shown. Blue circles with crosses represent model components. The minimum contour level in any given map is three times the rms noise. The labels "C" and "J" denote cores and jet components, respectively. We numbered jet components sequentially from the core outward, with "J0" indicating a jet component newly launched between two observing epochs. Detailed information for parameters of each source is listed in Table 4.

Table 2
Global properties of the images of our target sources

| Source	Epoch	Frequency (GHz)	Total flux (Jy)	Peak (Jy/beam)	Image rms (mJy)	Beam size (mas×mas)	Image scale (pc/mas)
1055+018	2014-11-03	22	3.86	3.6	1.9	1.68 × 1.29	7.78
0133+476	2014-11-04	22	1.73	1.63	0.96	1.5 × 1.06	7.7
1642+690	2014-10-22	22	0.87	0.61	0.99	1.34 × 1.15	7.35
3C120	2014-11-05	22	1.65	1.45	1.23	1.44 × 1.15	0.65
3C84	2014-11-03	22	21.88	10.1	17.4	1.43 × 1.04	0.35
BL LAC	2014-10-22	22	3.2	2.54	2.33	1.1 × 0.873	1.29
	2015-03-31	22	2.01	1.54	2.71	1.13 × 1.04	
	2014-04-17	43	3.43	2.86	3	0.648 × 0.528	
	2015-04-01	43	1.96	1.45	0.92	0.638 × 0.601	
3C111	2014-10-23	22	2.64	1.7	0.93	1.28 × 1.14	0.95
	2015-04-01	22	1.93	1.17	1.6	1.24 × 1.08	
	2014-03-15	43	1.68	1.06	1.05	0.666 × 0.602	
	2015-04-02	43	1.5	1.01	1.93	0.613 × 0.526	
3C345	2015-03-31	22	2.76	1.91	3.7	1.05 × 1.01	6.63
	2015-04-01	43	2.07	1.63	1.55	0.655 × 0.613	
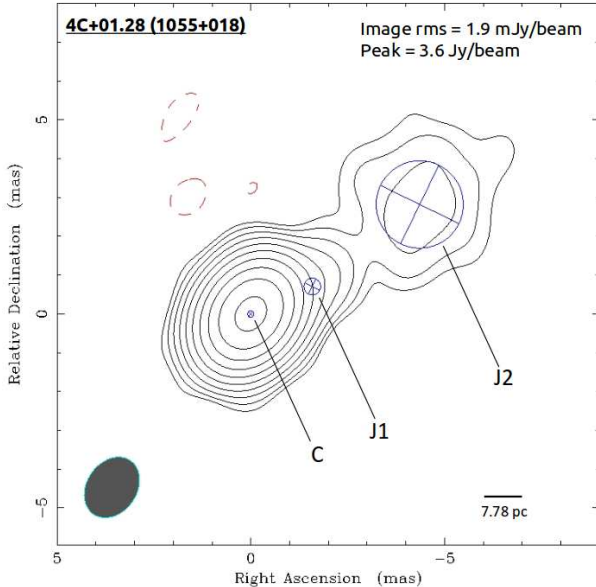
Figure 1. 1055+018 (4C+01.28) at 22 GHz. The synthesized beam and the angular scale are shown in the bottom-left-corner and bottom-right-corner, respectively. The image rms and peak intensity is indicated in the top-right-corner. The minimum contour level is 3 times of image rms. Blue circles with crosses are Gaussian model fitted jet components. The label "C" denotes the radio core, "J" represents jet components. Jet components are numbered in order of position from the core.

3.1. 1055+018 (4C+01.28)

1055+018 (4C+01.28) is a quasar with a redshift of 0.888 (Shaw et al. 2012). The corresponding angular scale is 7.78 pc/mas. Lister et al. (2013) found a maximum apparent jet speed of $8.05c$ (with c being the speed of light) based on four epochs of Very Long Baseline Array (VLBA) 15.4 GHz observations obtained within the frame of the MOJAVE program from 1998 to 2003. In our data (shown in Figure 1), 1055+018 shows a core-
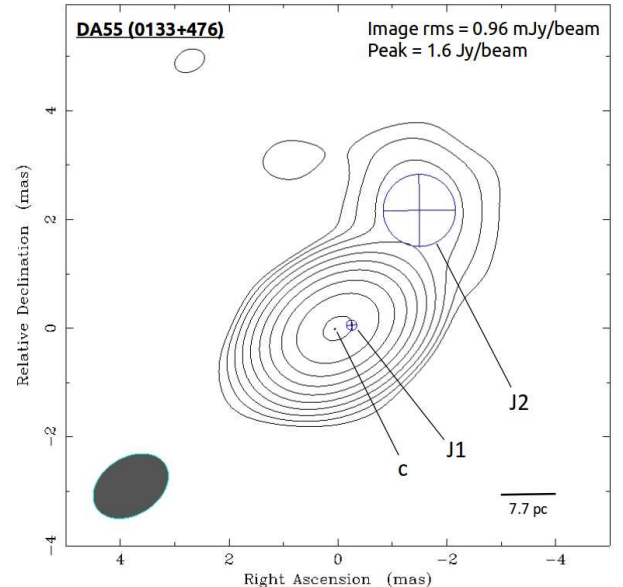

Figure 2. 0133+476 (DA55) at 22 GHz. Indicators are the same as in Figure 1.

dominated structure and a bulky jet in north-western direction. The jet is extended up to ∼7 mas. The total flux of the entire source is 3.86 Jy with a peak intensity of 3.6 Jy/beam. Including the core, three model components can be found. Since the MOJAVE program stopped monitoring this source in October 2012, our map is one of the most recent high-resolution images of 1055+018 (the most recent observation being from December 2014 by the Boston University blazar monitoring VLBA program at 43 GHz).

3.2. 0133+476 (DA55)

Figure 2 shows 0133+476 (DA 55), a flat-spectrum radio quasar (FSRQ) with a redshift of 0.859 (similar to 1055+018). The corresponding angular scale is 7.7
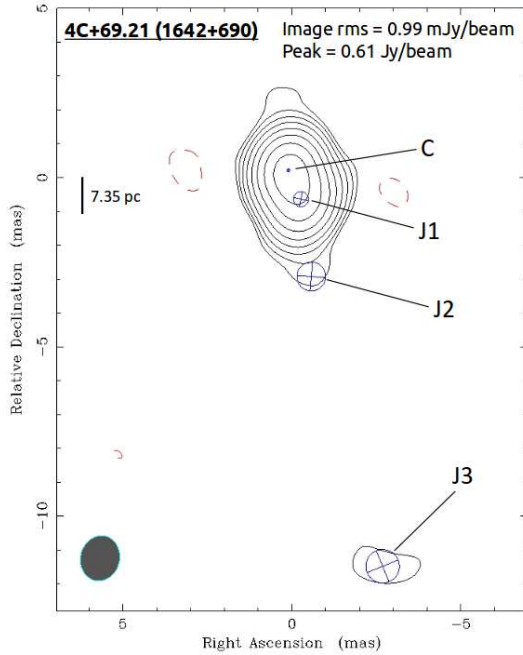
Figure 3. 1642+690 (4C+69.21) at 22 GHz. The angular scale is indicated on the left. Everything else is the same as in Figure 1.

Figure 4. 3C 120 at 22 GHz. Indicators are the same as in Figure 1.

pc/mas. The source is also known as a γ-ray emitter (cf., Nagai et al. 2013, and references therein). Lister et al. (2013) found a maximum apparent jet speed of 15.4c. Our map shows a jet in north-west direction extending out to ~4 mas. The jet shows a rather continuous shape; this indicates that the angular resolution of KaVA at 22 GHz is not enough to resolve the detailed structure. Even though, we were able to detect three model components (including the core). The total flux of the source is 1.73 Jy, with a peak intensity of 1.63 Jy/beam. Like for 1055+018, monitoring on this source by the MOJAVE program stopped in July 2013.

3.3. 1642+690 (4C+69.21)

1642+690 (4C+69.21), shown in Figure 3, is a radio loud quasar with a redshift of 0.751 (Lawrence et al. 1986). The corresponding angular scale is 7.35 pc/mas. Several works reported that the source shows apparent superluminal jet with a speed of 9c (Venturi et al. 1997; Lister et al. 2013). In our data, we only found a core-dominated morphology with a very faint jet component south of the core, approximately ~12 mas from the core. Even though the detailed source structure is not resolved, we found four model components that are expanding along the jet. 1642+690 has a total flux of 0.87 Jy with a peak intensity of 0.61 Jy/beam, making it the faintest among our targets. The MOJAVE program stopped observations of this source in September 2012.

3.4. 3C 120

3C 120 (Figure 4) is well known for its extended structure toward the south-west. The source is classified
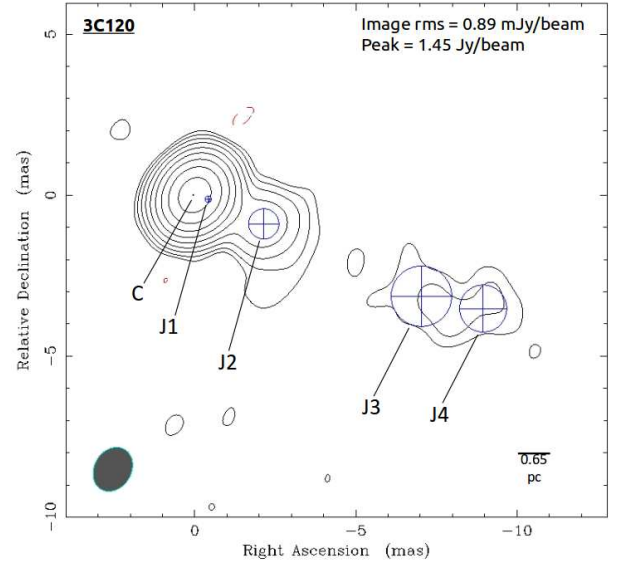
as radio galaxy with a redshift of 0.033 (Michel & Huchra 1988), corresponding to an angular scale of 0.65 pc/mas. Our map shows an extended jet reaching out to more than 10 mas from the core. 3C 120 has been studied with respect to its γ-ray emission (e.g., Sahakyan et al. 2015; Casadio et al. 2015) and its polarization (e.g., Gómez et al. 2008, and references therein). Here, we focus on its jet kinematics. The known maximum apparent jet speed is 6.43c (Lister et al. 2013). With additional data from future KaVA observation, we expect to trace the motion of the jet components and to test its kinematics. We were able to detect five model components, which also shows a general trend of increasing size as function of distance from the core. The total flux of the source is 1.65 Jy, with a peak intensity of 1.45 Jy/beam.

3.5. 3C 84

3C 84 (Figure 5) might well be one of the most "popular" radio galaxies in radio astronomy since it greatly increased its activity starting in 2005 (Abdo et al. 2009), and is the brightest source among our targets (21.88 Jy in total flux, 10.1 Jy/beam in peak intensity). As already noted by previous studies (e.g., Nagai et al. 2014, and references therein), the jet component J3, which is located ~2 mas south of the core, is brighter than the core itself (causing the phase center of our map to be placed onto J3). Given its brightness, we used 3C 84 as amplitude calibrator in our observations whenever it was available. It is well known that 3C 84 is effectively unpolarized, probably due to strong Faraday depolarization (Walker et al. 2000; Trippe et al. 2012) (accordingly, 3C 84 was used as a polarimetric calibrator in PAGaN I). Since it keeps being observed as a calibrator for other targets, we excluded 3C 84 from dedicated observations in 2015. 3C 84 has a redshift of 0.0176 (Strauss et al. 1992) and a corresponding angu-
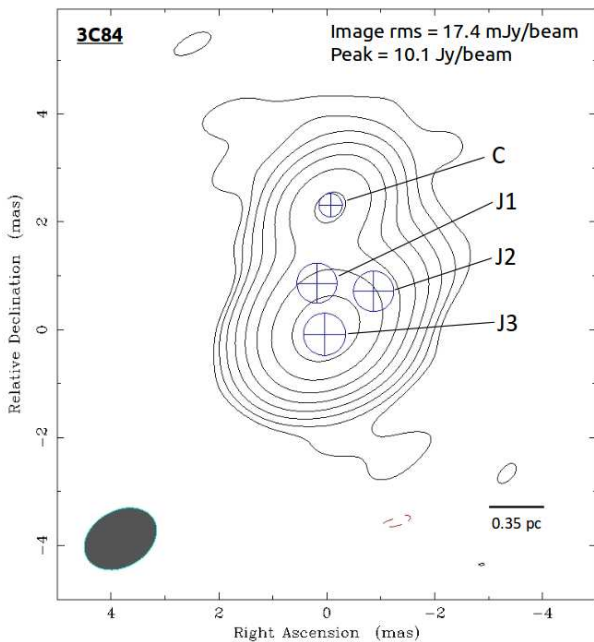
Figure 5. 3C 84 at 22 GHz. Indicators are the same as in Figure 1. The map center is placed onto the brightest component J3, not the core.

lar resolution of 0.35 pc/mas, making it the closest of our targets.

3.6. BL Lac

BL Lac (2200+420) has a redshift of 0.0686 (Vermeulen et al. 1995), which corresponds to an angular scale of 1.29 pc/mas. We were able to obtain four deep high resolution images (Figure 6) at 22 and 43 GHz in 2014 and 2015. In 2015, quasi-simultaneous dual-frequency observations were possible. The source is characterized by its extended and complicated jet structure toward the south. BL Lac shows significant changes in the total flux and map peak within about one year, as well as in the morphology of the jet. The total flux was 3.2 Jy in 2014 and 2.01 Jy in 2015 at 22 GHz, and 3.43 Jy and 1.96 Jy at 43 GHz. We found 5–7 jet components in each map.

3.7. 3C 111

As for BL Lac, we obtained four images of 3C 111 in total (Figure 7). 3C 111 is a radio galaxy with a redshift of 0.491 (Eracleous & Halpern 2004). The corresponding angular scale is 0.95 pc/mas. A long jet, which extends up to ∼10 mas in north-east direction, can be found in each image. In the 43 GHz maps several knotty features are visible which are not distinguishable at 22 GHz. 5–6 model components can be found. The total flux of BL Lac was 2.64 Jy in 2014 and 1.93 in 2015 at 22 GHz, and 1.68 Jy and 1.5 Jy at 43 GHz.

3.8. 3C 345

3C 345 is a quasar with a redshift of 0.593 (Marziani et al. 1996). We included this source in our target list in

2015 as a replacement for 3C 84. Although 3C 345 has relatively high redshift compared to our other targets, it clearly shows its detailed jet structure in our KaVA maps. 3C 345 has been a "popular" object of study since the 1960s (e.g., Goldsmith & Kinman 1965); here, we focus on features like superluminal motion of the jet and evolution of the spectral index. Our results are shown in Figure 8. 3C 345 shows a complicated jet structure that extends out to ∼9 mas toward the west. The jet appears to bend at a distance of ∼1.5 mas from the core. The separate large jet component ∼5 mas west of the core shows a knotty structure. 3C 345 has a total flux of 2.76 Jy with a peak intensity of 1.91 Jy/beam at 22 GHz (2.07 Jy and 1.63 Jy/beam at 43 GHz). We were able to resolve four model components (including the core) at 22 GHz and found one more component at 43 GHz which seems to be a recently launched component that has not been resolved by the 22 GHz observations.

4. DISCUSSION

4.1. Spectral Index

AGN jets are known to be emitters of continuous synchrotron emission which follows a powerlaw spectrum. The corresponding spectral index α is given by

$$S_\nu \propto \nu^\alpha \qquad (1)$$

where S_ν is the flux density observed at frequency ν. The spectrum is approximately flat ($\alpha \gtrsim -0.5$) in optically thick emission regions and steep ($\alpha \lesssim -0.5$) in optically thin regions. For AGN in general, the core region is optically thick, while jets tend to become optically thinner as they expand on their way outward. Among our targets, BL Lac, 3C 111, and 3C 345 were observed simultaneously at both 22 and 43 GHz in 2015. We created a spectral index map for each source using the Python routine VIMAP which matches two radio maps obtained at different frequencies by using two-dimensional correlation (Kim & Trippe 2014).

Figure 9, 10, and 11 are the spectral index maps for all three sources using the 22 and 43 GHz maps. We assumed that the core-shift effect (Porcas 2009) is negligible at our observing frequencies. In general, as expected, the maps show flat spectral index values in the core regions and increasingly steep indices along the jets. This is especially obvious in case of 3C 345, with values as small as $\alpha \approx -2$ in the outermost parts of the jet. The steep spectral index in jet of 3C 345 is also consistent with previous studies (e.g., Ros et al. 2000; Lobanov & Zensus 1999; Rantakyroe et al. 1995). Coincidentally, BL Lac, 3C 111, and 3C 345 correspond to three different AGN types (a BL Lac object, a radio galaxy, and a quasar, respectively). Initially, all sources show flat cores. BL Lac shows $\alpha \approx 0$ also along the jet down to ∼3 mas from the core, 3C 111 has a moderately steep ($\alpha \approx -1$) spectral index throughout the jet, and 3C 345 shows a very steep ($\alpha \approx -2$) outermost jet component. This sequence – flat (BL Lac object)
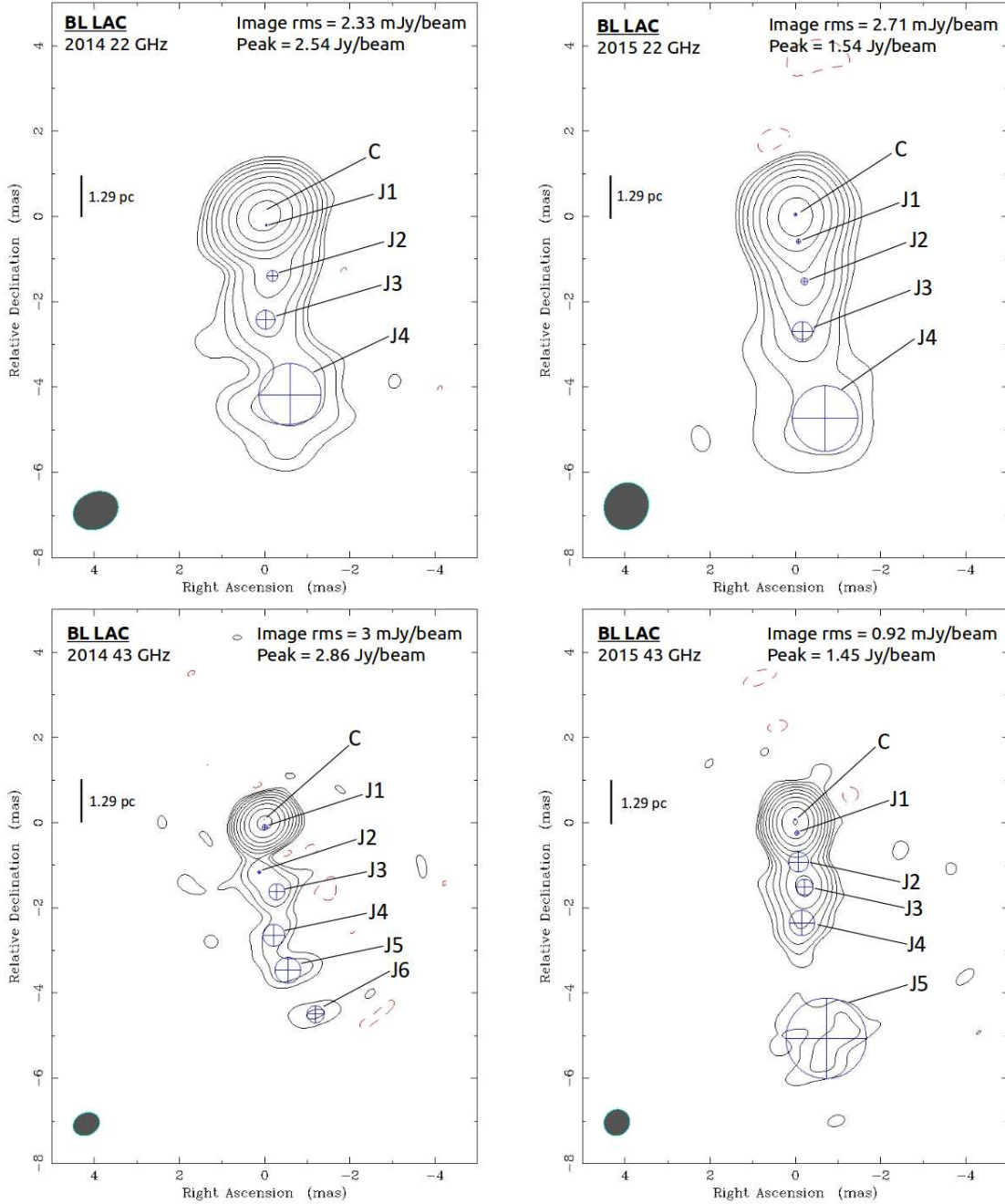
Figure 6. Maps of BL Lacertae. *Top left:* At 22 GHz in October 2014. *Top right:* At 22 GHz in March 2015. *Bottom left:* At 43 GHz in April 2014. *Bottom right:* At 43 GHz in April 2015. Indicators are the same as in Figure 3.

→ moderate steep (radio galaxy) → steep (quasar) – could be caused by different viewing angles.

4.2. Kinematics of Jet Components

In the cases of BL Lac and 3C 111, we were able to trace the motion of their jets between 2014 and 2015.

4.2.1. BL Lac

We matched core and jet components in the BL Lac 22 GHz data (Figure 12) and found the jet components propagating toward the south. The time between both

observations was 161 days. Components J1–J4 moved between 0.067 and 0.62 parsec, which corresponds to apparent speed from $0.5c$ to $4.6c$ (Table 3).

The relation between the apparent speed β_{app} and the jet orientation θ can be expressed by

$$\beta_{\mathrm{app}} = \frac{\beta \sin \theta}{1 - \beta \cos \theta} \qquad (2)$$

where β is the intrinsic velocity in units of the speed of light and θ is the angle between the line of sight and the jet (e.g., Kellermann et al. 2007). We show the
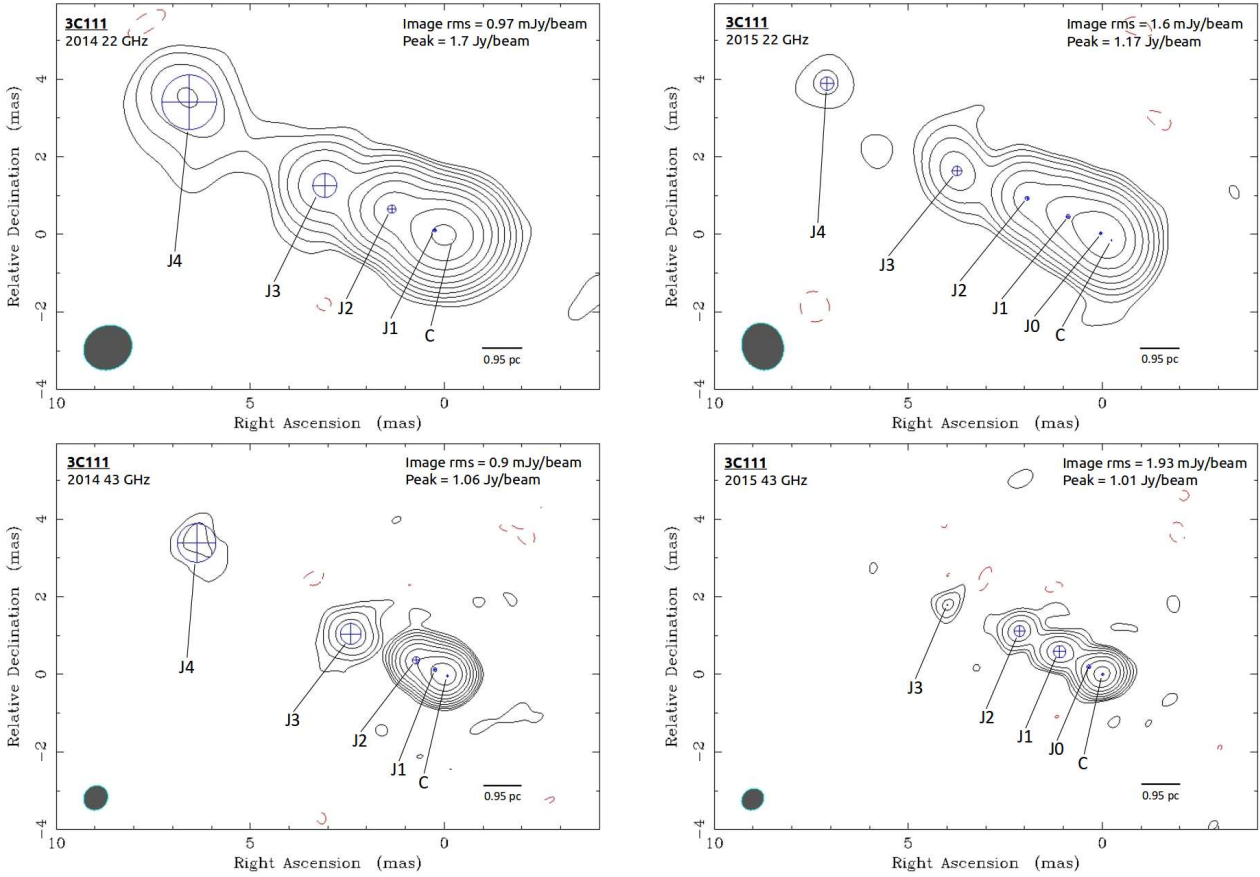
Figure 7. Maps of 3C 111. *Top left:* At 22 GHz in October 2014. *Top right:* At 22 GHz in April 2015. *Bottom left:* At 43 GHz in March 2014. *Bottom right:* At 43 GHz in April 2015. Indicators are the same as in Figure 1.
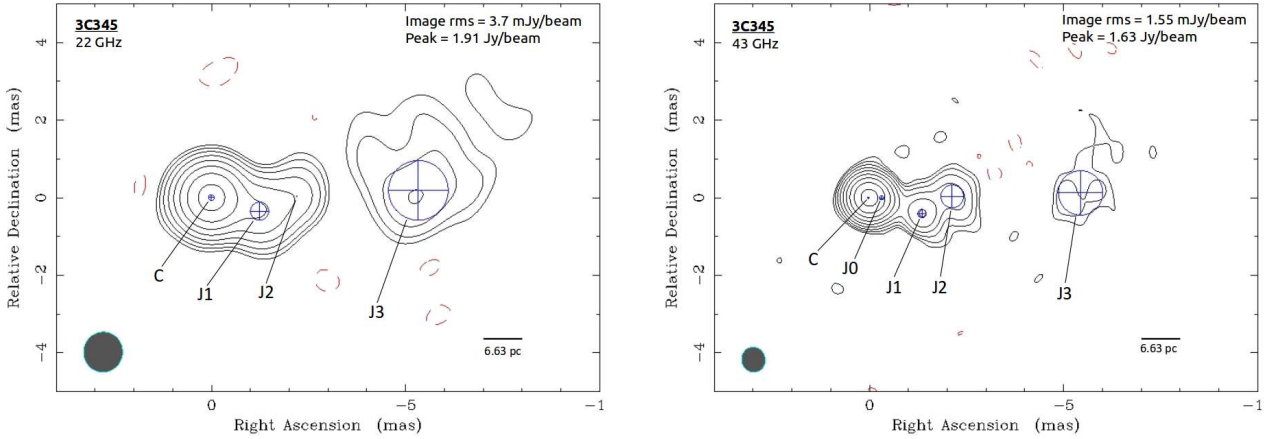

Figure 8. Maps of 3C 345 obtained in March/April 2015. *Left:* At 22 GHz. *Right:* At 43 GHz. Indicators are the same as in Figure 1.

apparent speed as function of viewing angle in Figure 14 for several values of β (0.5, 0.9, 0.95, 0.98, 0.99, 0.995, 0.998 and 0.999). As one can read off the diagram in a straightforward manner, an apparent speed $\beta_{app} \approx 5c$ (dashed line in the diagram) implies a lower limit for the intrinsic speed of $\sim 0.98c$ (lime line) and an upper limit of the viewing angle of $\sim 20°$. We note the ambiguity in viewing angle which could have very small values of a few degrees. However, we consider such small angles

unlikely for BL Lac (and also for 3C 111 – cf., Section 4.2.2) because we would expect the jet to be optically thick along its entire length in this case, in contradiction to the distribution shown by the spectral index map.

In the 43 GHz data, we were not able to cross-identify individual components due to poor quality of the 2014 data. Furthermore, substantial changes in both morphology and physical properties (like total flux: $\sim 40\%$ decreased; peak intensity: $\sim 50\%$ decreased) occurred
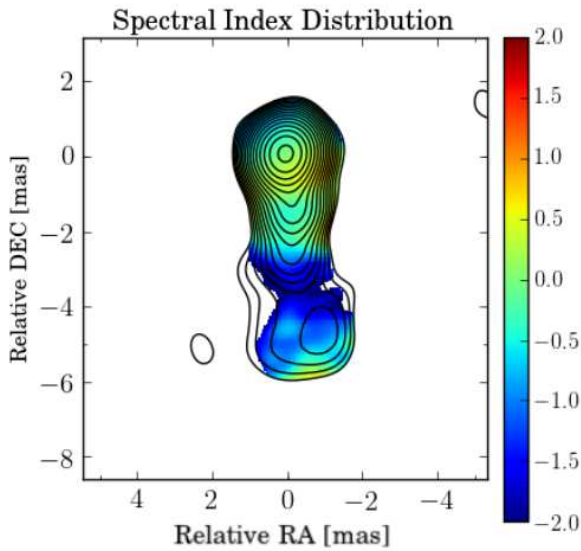
Figure 9. Spectral index map of BL Lac. The color bar on the right indicates a spectral index α from -2 to $+2$.
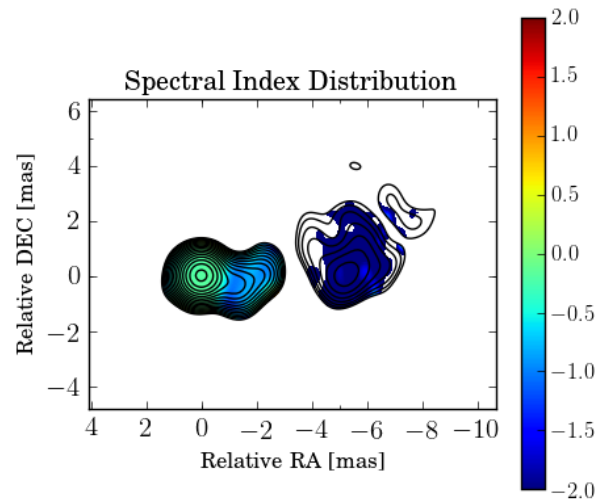

Figure 11. Spectral index map of 3C 345. The color bar on the right indicates a spectral index α from -2 to $+2$.
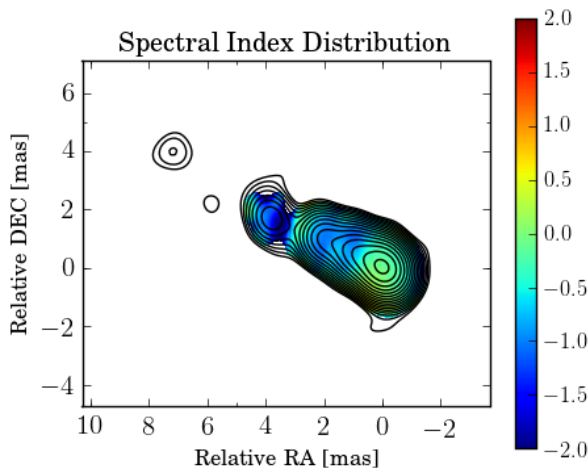

Figure 10. Spectral index map of 3C 111. The color bar on the right indicates a spectral index α from -2 to $+2$.
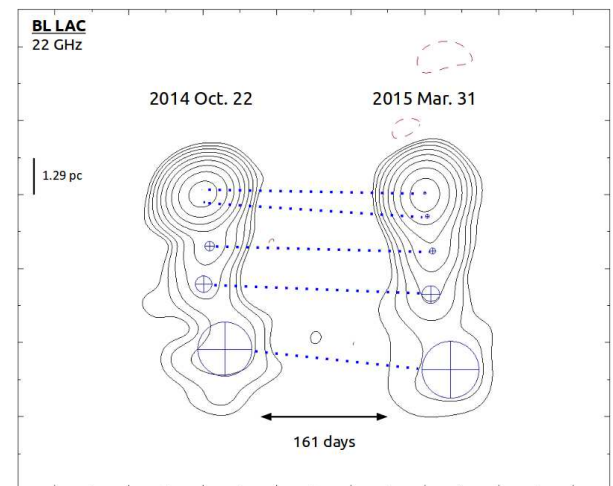

Figure 12. Evolution of BL Lac between 2014 and 2015 at 22 GHz. Five model components can be matched (blue dashed lines).

within the 350 days passed between the two 43 GHz datasets, further complicating the comparison.

4.2.2. 3C 111

Figure 13 shows the comparison between observations of 3C 111 obtained in 2014 and 2015. At 22 GHz, the time gap between the two observations is 161 days. We assumed that the first model component (marked by a red arrow) in the 2015 map, which is located just next to the core, is a newly launched jet component. We matched the remaining four components and calculated the distance over which they moved. Components J0–J4 moved between 0.31 and 0.76 parsec, corresponding to a (average) apparent speed of around 4.6c (Table 3).

We applied the same approach to our 43 GHz data. We identified component J0 in the 2015 map as a newly launched jet component and matched the components

J1–J3. J4 was not detected in 2015. At 43 GHz, the time span between the maps is 384 days. Else than for the 22 GHz data, we find travel distances ranging from 0.93 pc to 1.66 pc; the further the component is located from the core, the larger distance it moved. Apparent speeds range from 2.9c to 5.2c. Our results

In order to confirm the motion of the jets and to check our analysis, we repeated our analysis with 15.4 GHz VLBA data from the MOJAVE program. Although observation frequencies and epochs are different, we were able to make a reasonable comparison to our data. We picked MOJAVE maps obtained on 2014 May 12, 2014 December 12, and 2015 May 18, which is about one month delayed compared to our observations. The time spans covered are 158 and 372 days, respectively. The propoer motions of jet components in the MOJAVE maps (Figure 13, bottom panels) are consistent with
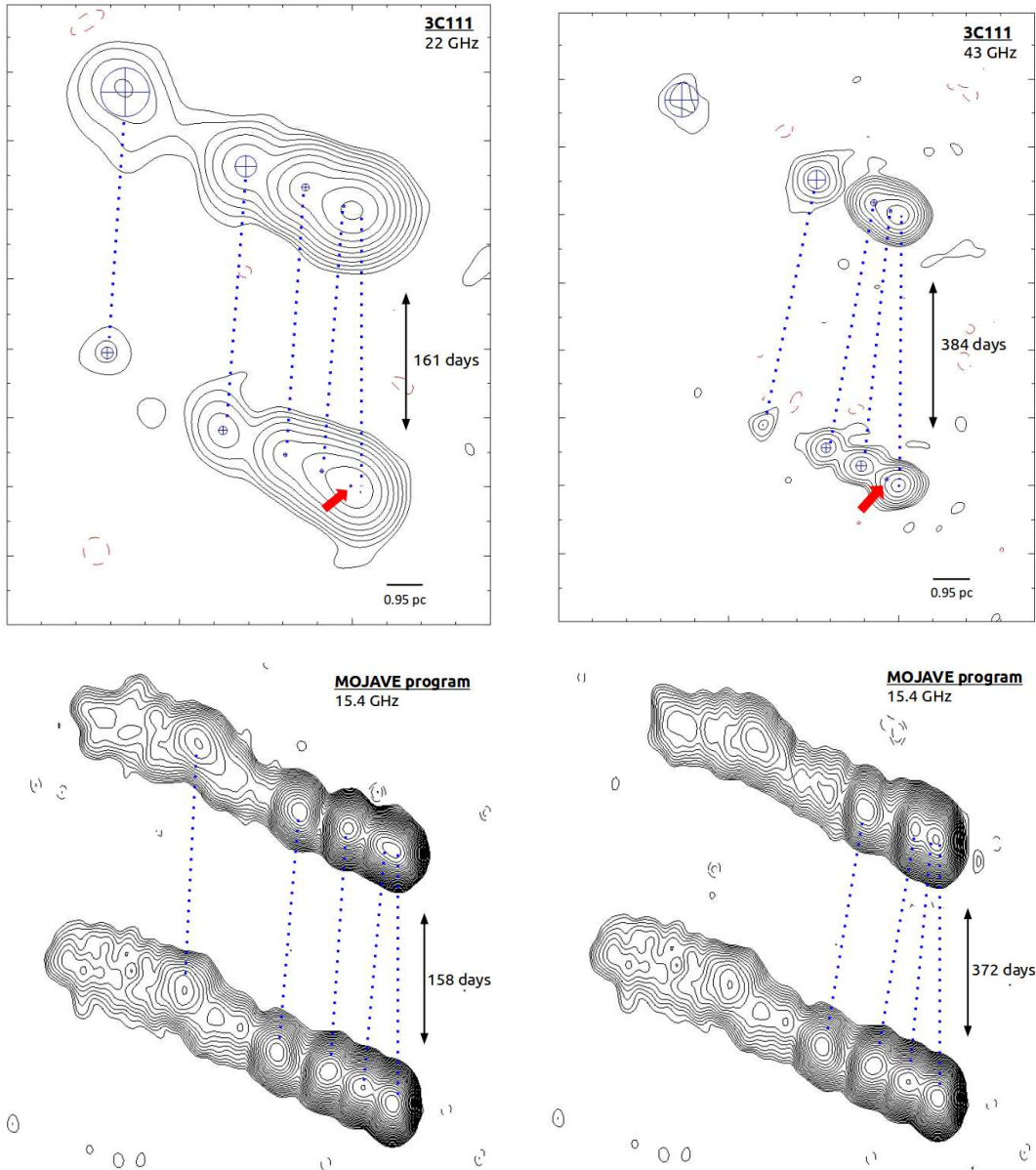
Figure 13. Time-resolved VLBI maps of 3C 111 obtained by us with KaVA (top panels) and by the MOJAVE program with the VLBA (bottom panels). *Top left:* Comparison of 22-GHz KaVA maps from 2014 and 2015. We assumed that a new jet component was launched in 2015 (red arrow, J0 in Figure 7 top right), and matched five model components visible in both epochs (blue dashed lines). *Top right:* Comparison of 43-GHz KaVA maps from 2014 and 2015. We assumed that a new jet component ws in 2015 (red arrow, J0 in Figure 7 bottom right), and matched four model components visible in both epochs (blue dashed lines). *Bottom left:* MOJAVE images obtained at 15.4 GHz, observed on 12 December 2014 (top) and 18 May 2015 (bottom). We re-identified and matched the same jet components as in the 22-GHz KaVA maps. *Bottom right:* MOJAVE images obtained at 15.4 GHz, observed on 12 May 2014 (top) and 18 May 2015 (bottom). We re-identified and matched the same jet components as in the 43 GHz KaVA maps. The results by KaVA and MOJAVE are in good agreement.

our results based on KaVA data.

4.3. Jet Expansion

As noted several times throughout Section 3, our maps indicate a trend toward more extended jet components at larger core distances, as expected for expanding jets. When combining the data for all sources at all frequencies and all epochs in a common diagram, one finds the

result illustrated in Figure 15. Indeed, one finds larger component sizes d for larger core distances r. Remarkably, all data approximately follow the same relation $d \approx 0.2r$, albeit within large scatter. This is in good agreement with global jet expansion; however, we note that this relation comes with substantial systematic uncertainties because we average over sources with different viewing angles and jet kinematics. At the very least,
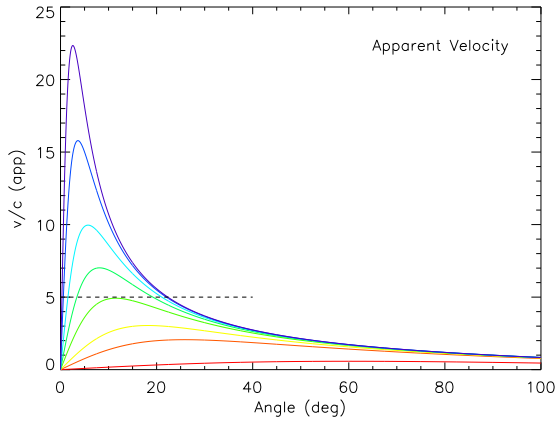
Figure 14. Apparent speed as a function of jet orientation for various values of β. From the top, β=0.999 (purple), β=0.998 (blue), β=0.995 (cyan), β=0.99 (green), β=0.98 (lime), β=0.95 (yellow), β=0.9 (orange) and β=0.5 (red). The black dashed line, which touches the peak of the lime line (β=0.98), indicates an apparent speed of $5c$.

Table 3
Apparent speed of jet components of BL Lac and 3C 111

ID	Distance moved (pc)	β_{app} (c)
BL LAC 22 GHz:		
J1	0.385	2.85
J2	0.067	0.49
J3	0.301	2.23
J4	0.620	4.59
3C 111 22 GHz:		
J0	0.312	2.31
J1	0.728	5.38
J2	0.647	4.78
J3	0.757	5.60
J4	0.705	5.21
3C 111 43 GHz:		
J0	0.387	1.20
J1	0.845	2.62
J2	1.431	4.44
J3	1.578	4.89

we demonstrated that already few epochs of KaVA data are able to identify universal properties of AGN jets.

5. CONCLUSIONS

We presented first results from KaVA observations of eight radio-bright AGN conducted in the frame of our *P*lasma-physics of *A*ctive *Ga*lactic *N*uclei (PAGaN) project. Our main results are:

1. We obtained interferometric maps sufficient to identify individual source components, with numbers of components (core plus jet components) ranging from three (for $1055+015$ and $0133+476$) to seven (for BL Lac at 43 GHz).

2. We observed significant proper motions of jet components in BL Lac and 3C 111. In both sources,
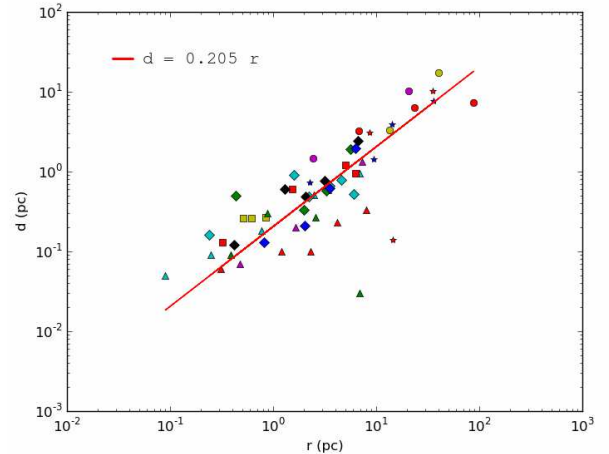

Figure 15. Jet component size d vs. distance from core r, in units of parsec, for all available data sets. Markers indicate $1055+018$ (yellow circle), $0133+476$ (magenta circle), $1642+690$ (red circle), 3C 120 (red square), 3C 84 (yellow square), 3C 111 (triangle: magenta – 2014 22 GHz, cyan – 2014 43 GHz, red – 2015 22 GHz, green – 2015 43 GHz), BL Lac (diamond: green – 2014 22 GHz, cyan – 2014 43 GHz, blue – 2015 22 GHz, black – 2015 43 GHz) and 3C 345 (star: red – 22 GHz, blue – 43 GHz). The data follow a global relation $d \approx 0.2r$.

we found superluminal apparent jet speeds up to about about $5c$, thus constraining the intrinsic speeds to $\beta \gtrsim 0.98c$ and the jet viewing angles to $\theta \lesssim 20°$.

3. The spectral index maps for BL Lac, 3C 111, and 3C 345 show a tendency for an increasingly fast steepening of the spectral index as function of core distance in the order BL Lac object → radio galaxy → quasar. This is probably caused by systematic differences in viewing angle.

4. Jet components show systematically larger diameters d at larger core distances r. Notably, the components of our targets all follow the same universal relation $d \approx 0.2r$, albeit within substantial scatter.

Our results demonstrate the value of KaVA for studies of the physics of active galactic nuclei. Even though our observations already provided a wealth of information, further observations will be necessary. Additional quasi-simultaneous dual-frequency observations will uncover temporal variability of spectral index maps due to jet propagation. Additional component position measurements will be important for constraining the speeds and possible non-linear motions of jet components. Overall, we may expect additional discoveries from a systematic plasma-physical study of AGN – as intended by the PAGaN project.

Table 4
Parameters for model components

Source ID	S_{Tot} (Jy)	σ_{Tot} (mJy)	S_{Peak} (Jy/beam)	σ_{Peak} (mJy/beam)	r (pc)	σ_r (pc)	θ (°)	σ_θ (°)	d (pc)	σ_d (pc)
1055+018										
22 GHz:										
C	3.64	176.04	3.62	87.75	—	—	—	—	0.17	0.032
J1	0.08	14.3	0.07	6.93	13.53	0.16	−65.91	0.012	0.43	0.31
J2	0.11	27.22	0.04	7.43	40.41	1.62	−57.09	0.04	2.25	3.25
0133+476										
22 GHz:										
C	1.35	103.88	1.35	52	—	—	—	—	0.03	0.009
J1	0.32	44.57	0.32	22.04	2.45	0.05	−76.79	0.021	0.19	0.1
J2	0.046	13.7	0.023	4.56	20.63	1.02	−35.46	0.049	1.33	2.04
1642+690										
22 GHz:										
C	0.51	31.99	0.51	15.99	—	—	—	—	0.09	0.021
J1	0.35	40.35	0.31	19.1	6.81	0.1	−156.63	0.015	0.44	0.2
J2	0.004	3.88	0.004	1.89	23.58	1.52	−167.9	0.065	0.85	3.05
J3	0.006	4.68	0.004	2.03	88.36	1.67	−166.61	0.019	0.99	3.34
3C 120										
22 GHz:										
C	1.31	78.58	1.31	39.34	—	—	—	—	0.04	0.001
J1	0.22	17.37	0.21	8.62	0.32	0.003	−106.39	0.008	0.2	0.005
J2	0.08	19.85	0.05	8.08	1.54	0.05	−112.45	0.029	0.94	0.09
J3	0.021	12.8	0.009	3.87	5.04	0.25	−113.98	0.05	1.88	0.51
J4	0.019	10.48	0.009	3.39	6.29	0.18	−111.43	0.029	1.46	0.36
3C 84										
22 GHz:										
C	4.1	460.55	3.71	218.88	—	—	—	—	0.43	0.009
J1	2.55	442.3	1.89	188.42	0.51	0.013	170.09	0.025	0.74	0.026
J2	1.64	247.01	1.22	105.25	0.62	0.011	−153.39	0.018	0.75	0.023
J3	13.39	1301.13	9.71	546.98	0.84	0.008	177.33	0.009	0.78	0.015
BL Lac 2014										
22 GHz:										
C	1.75	84.72	1.75	42.38	—	—	—	—	0.01	0.0002
J1	1.02	108.17	1.02	54.01	0.43	0.001	−170.06	0.003	0.04	0.003
J2	0.17	29.22	0.16	14.18	1.97	0.015	−172.36	0.008	0.26	0.03
J3	0.09	21.77	0.074	9.87	3.28	0.038	−179.1	0.012	0.44	0.076
J4	0.16	68.32	0.045	14.69	5.61	0.31	−171.87	0.055	1.46	0.62
43 GHz:										
C	1.67	97.82	1.67	48.88	—	—	—	—	0.02	0.001
J1	1.46	86.82	1.41	42.67	0.24	0.002	−176.24	0.01	0.12	0.005
J2	0.06	24.29	0.06	12.34	1.6	0.009	174.6	0.006	0.07	0.018
J3	0.1	35.36	0.069	14.46	2.22	0.051	−170.27	0.023	0.38	0.102
J4	0.044	23.45	0.027	8.91	3.52	0.11	−175.28	0.031	0.51	0.22
J5	0.051	23.72	0.026	8.09	4.62	0.12	−171.11	0.026	0.61	0.24
J6	0.028	12.29	0.02	5.16	6.1	0.07	−165.27	0.011	0.4	0.13
BL Lac 2015										
22 GHz:										
C	1.45	62.53	1.45	31.27	—	—	—	—	0.07	0.002
J1	0.21	44.56	0.21	22.35	0.81	0.007	−173.93	0.009	0.1	0.014
J2	0.19	77.34	0.19	39.12	2.04	0.021	−172.4	0.01	0.16	0.042
J3	0.077	14.21	0.065	6.49	3.55	0.031	−176.61	0.009	0.48	0.062
J4	0.083	34.4	0.028	8.75	6.23	0.31	−171.72	0.049	1.54	0.62
43 GHz:										
C	1.18	103.94	1.17	51.8	—	—	—	—	0.03	0.002
J1	0.5	53.04	0.49	26.23	0.42	0.003	−172.11	0.008	0.1	0.007
J2	0.05	13.8	0.03	5.35	1.3	0.051	−175.11	0.039	0.47	0.102
J3	0.14	14.7	0.11	6.28	2.07	0.015	−171.76	0.007	0.38	0.029
J4	0.043	12.37	0.023	4.31	3.14	0.072	−176.15	0.023	0.6	0.14
J5	0.056	27.32	0.009	3.71	6.7	0.51	−171.87	0.076	1.89	1.02

Table 4

Continued

Source ID	S_{Tot} (Jy)	σ_{Tot} (mJy)	S_{Peak} (Jy/beam)	σ_{Peak} (mJy/beam)	r (pc)	σ_r (pc)	θ (°)	σ_θ (°)	d (pc)	σ_d (pc)
3C 111 2014										
22 GHz:										
C	1.01	38.39	1.02	19.28	—	—	—	—	0	0
J1	0.91	28.64	0.91	14.33	0.48	0.001	62.38	0.001	0.08	0.001
J2	0.54	45.17	0.53	22.35	1.66	0.004	63.48	0.003	0.21	0.009
J3	0.11	13.84	0.092	6.21	3.39	0.02	67.09	0.006	0.62	0.04
J4	0.055	21.51	0.026	6.83	7.27	0.18	62.48	0.024	1.41	0.35
43 GHz:										
C	0.85	109.17	0.84	54.4	—	—	—	—	0.05	0.003
J1	0.47	83.05	0.46	40.98	0.34	0.004	63.12	0.012	0.1	0.008
J2	0.28	38.91	0.26	18.71	0.87	0.006	63.54	0.007	0.19	0.013
J3	0.06	18.73	0.038	7.19	2.59	0.048	66.5	0.019	0.54	0.1
J4	0.021	9.55	0.007	2.43	6.95	0.16	62.06	0.023	1	0.32
3C 111 2015										
22 GHz:										
C	0.52	26.11	0.52	13.07	—	—	—	—	0.03	0.001
J0	0.67	31.43	0.66	15.7	0.31	0.001	57.2	0.002	0.07	0.002
J1	0.44	54	0.44	26.97	1.21	0.003	61.47	0.002	0.1	0.006
J2	0.21	15.24	0.21	7.59	2.3	0.002	63.53	0.001	0.1	0.004
J3	0.06	14.86	0.06	7.23	4.14	0.014	65.88	0.003	0.25	0.028
J4	0.013	3.59	0.012	1.74	7.95	0.024	61.16	0.003	0.34	0.047
43 GHz:										
C	0.98	114.19	0.97	56.86	—	—	—	—	0.05	0.003
J0	0.17	36.19	0.17	17.78	0.39	0.005	61.76	0.013	0.1	0.01
J1	0.21	52.42	0.16	22.61	1.19	0.021	62.27	0.018	0.32	0.042
J2	0.1	18.66	0.081	8.36	2.3	0.014	62.54	0.006	0.28	0.028
J3	0.027	9.84	0.028	5	4.16	0.003	65.89	0.001	0.03	0.006
3C 345										
22 GHz:										
C	1.94	164.36	1.9	81.38	—	—	—	—	0.15	0.042
J1	0.43	53.42	0.36	24.46	8.57	0.11	−105.69	0.012	0.47	0.21
J2	0.13	28.42	0.13	14.28	14.63	0.008	−89.08	0.001	0.02	0.015
J3	0.28	110.16	0.08	24.82	35.4	1.58	−87.98	0.045	1.54	3.15
43 GHz:										
C	1.53	58.74	1.53	29.39	—	—	—	—	0.04	0.005
J1	0.17	27.41	0.16	13.07	9.54	0.06	−106.38	0.006	0.22	0.12
J0	0.21	48.78	0.21	23.98	2.26	0.043	−90.35	0.019	0.11	0.087
J2	0.1	30.56	0.06	10.93	14.31	0.38	−89.01	0.027	0.59	0.76
J3	0.052	32.05	0.02	8.72	36.26	1.69	−88.69	0.047	1.15	3.38

References

Abdo, A. A., Ackermann, M., Ajello, M., et al. 2009, Fermi Discovery of Gamma-Ray Emission from NGC 1275, ApJ, 699, 31

Bartel, N., Herring, T. A., Ratner, M. I., et al. 1986, VLBI Limits on the Proper Motion of the 'Core' of the Superluminal Quasar 3C 345, Nature, 319, 733

Beckmann, V., & Shrader, C. R. 2012, Active Galactic Nuclei (Weinheim: Wiley-VCH)

Blandford, R. D., & Znajek, R. L. 1977, Electromagnetic Extraction of Energy from Kerr Black Holes, MNRAS, 179, 433

Boettcher, M., Harris, D. E., & Krawczynski, H. 2012, Relativistic Jets from Active Galactic Nuclei (Weinheim: Wiley-VCH)

Bregman, J. N., Glassgold, A. E., Huggins, P. J., et al. 1986, Multifrequency Observations of the Superluminal Quasar 3C 345, ApJ, 301, 708

Casadio, C., Gómez, J. L., Grandi, P., et al. 2015, The Connection between the Radio Jet and the Gamma-Ray Emission in the Radio Galaxy 3C 120, ApJ, 808, 162

Eracleous, M., & Halpern, J. P. 2004, Accurate Redshifts and Classifications for 110 Radio-Loud Active Galactic

Nuclei, ApJS, 150, 181

Ferrarese, L., & Ford, H. 2005, Supermassive Black Holes in Galactic Nuclei: Past, Present and Future Research, SSRv, 116, 523

Gómez, J. L., Marscher, A. P., Jorstad, S. G., et al. 2008, Faraday Rotation and Polarization Gradients in the Jet of 3C 120: Interaction with the External Medium and a Helical Magnetic Field?, ApJ, 681, L69

Goldsmith, D. W., & Kinman, T. D. 1965, The Optical Variability of 3C 345, ApJ, 142, 1693

Hovatta, T., Aller, M. F., Aller, H. D., et al. 2014, MOJAVE: Monitoring of Jets in Active Galactic Nuclei with VLBA Experiments. XI. Spectral Distributions, AJ, 147, 143

Jorstad, S. G., Marscher, A. P., Lister, M. L., et al. 2005, Polarimetric Observations of 15 Active Galactic Nuclei at High Frequencies: Jet Kinematics from Bimonthly Monitoring with the Very Long Baseline Array, AJ, 130, 1418

Kellermann, K. I., Kovalev, Y. Y., Lister, M. L., et al. 2007, Doppler Boosting, Superluminal Motion, and the Kinematics of AGN jets, Ap&SS, 311, 231

Kim, J.-Y., & Trippe, S. 2014, VIMAP: an Interactive Program Providing Radio Spectral Index Maps of Active Galactic Nuclei, JKAS, 47, 195

Kim, J.-Y., Trippe, S., Sohn, B. W., et al. 2015, PAGaN I: Multi-Frequency Polarimetry of AGN Jets with KVN, JKAS, 48, 285

Laing, R. A. 1980, A Model for the Magnetic-Field Structure in Extended Radio Sources, MNRAS, 193, 439

Lawrence, C. R., Pearson, T. J., Readhead, A. C. S., & Unwin, S. C. 1986, New Redshifts of Strong Radio Sources, AJ, 91, 494

Lee, S.-S., Lobanov, A. P., Krichbaum, T. P., et al. 2008, A Global 86 GHz VLBI Survey of Compact Radio Sources, AJ, 136, 159

Lee, S.-S., Oh, C. S., Roh, D.-G., et al. 2015, A New Hardware Correlator in Korea: Performance Evaluation Using KVN Observations, JKAS, 48, 125

Lee, S.-S., Petrov, L., Byun, D.-Y., et al. 2014, Early Science with the Korean VLBI Network: Evaluation of System Performance, AJ, 147, 77

Lister, M. L. 2005, The MOJAVE Program: Studying the Relativistic Kinematics of AGN Jets, ASPC, 340, 20

Lister, M. L., Aller, H. D., Aller, M. F., et al. 2009, MOJAVE: Monitoring of Jets in Active Galactic Nuclei with VLBA Experiments. V. Multi-Epoch VLBA Images, AJ, 137, 3718

Lister, M. L., Aller, M. F., Aller, H. D., et al. 2013, MOJAVE. X. Parsec-scale Jet Orientation Variations and Superluminal Motion in Active Galactic Nuclei, AJ, 146, 120

Lister, M. L., Cohen, M. H., Homan, D. C., et al. 2009, MOJAVE: Monitoring of Jets in Active Galactic Nuclei with VLBA Experiments. VI. Kinematics Analysis of a Complete Sample of Blazar Jets, AJ, 138, 1874

Lister, M. L., & Homan, D. C. 2005, MOJAVE: Monitoring of Jets in Active Galactic Nuclei with VLBA Experiments. I. First-Epoch 15 GHz Linear Polarization Images, AJ, 130, 1389

Lobanov, A. P., & Zensus, J. A. 1999, Spectral Evolution of the Parsec-Scale Jet in the Quasar 3C 345, ApJ, 521, 509

Marziani, P., Sulentic, J. W., Dultzin-Hacyan, D., et al. 1996, Comparative Analysis of the High- and Low-Ionization Lines in the Broad-Line Region of Active Galactic Nuclei, ApJS, 104, 37

Michel, A., & Huchra, J. 1988, Redshifts of Galaxies in the Winter Plane, PASP, 100, 1423

Nagai, H., Haga, T., Giovannini, G., et al. 2014, Limb-brightened Jet of 3C 84 Revealed by the 43 GHz Very-Long-Baseline-Array Observation, ApJ, 785, 53

Nagai, H., Kino, M., Niinuma, K., et al. 2013, The GENJI Programme: Gamma-Ray Emitting Notable AGN Monitoring by Japanese VLBI, PASJ, 65, 24

Nagai, H., Suzuki, K., Asada, K., et al. 2010, VLBI Monitoring of 3C 84 (NGC 1275) in Early Phase of the 2005 Outburst, PASJ, 62, L11

Niinuma, K., Lee, S.-S., Kino, M., et al. 2014, VLBI Observations of Bright AGN Jets with the KVN and VERA Array (KaVA): Evaluation of Imaging Capability, PASJ, 66, 103

O'Dea, C. P., Dent, W. A., Kinzel, W. M., & Balonek, T. J. 1986, Multifrequency Radio Observations of the Variable Quasars 0133+476, 0235+164, 1749+096, and 2131−021, AJ, 92, 1262

Porcas, R. W. 2009, Radio Astrometry with Chromatic AGN Core Positions, A&A, 505, L1

Rantakyroe, F. T., Baath, L. B., & Matveenko, L. 1995, Multiband VLBI imaging of the jet in 3C345., A&A, 293, 44

Readhead, A. C. S., Hough, D. H., Ewing, M. S., et al. 1983, Asymmetric Structure in the Nuclei of NGC 1275 and 3C 345, ApJ, 265, 107

Ros, E., Zensus, J. A., & Lobanov, A. P. 2000, Total intensity and polarized emission of the parsec-scale jet in 3C 345, A&A, 354, 55

Sahakyan, N., Zargaryan, D., & Baghmanyan, V. 2015, On the Gamma-Ray Emission from 3C 120, A&A, 574, A88

Shaw, M. S., Romani, R. W., Cotter, G., et al. 2012, Spectroscopy of Broad-line Blazars from 1LAC, ApJ, 748, 49

Strauss, M. A., Huchra, J. P., Davis, M., et al. 1992, A Redshift Survey of IRAS Galaxies. VII – The Infrared and Redshift Data for the 1.936 Jansky Sample, ApJS, 83, 29

Trippe, S., Krips, M., Piétu, V., et al. 2011, The Long-Term Millimeter Activity of Active Galactic Nuclei, A&A, 533, A97

Trippe, S., Bremer, M., Krichbaum, T. P., et al. 2012, A Search for Linear Polarization in the Active Galactic Nucleus 3C 84 at 239 and 348 GHz, MNRAS, 425, 1192

Unwin, S. C., Cohen, M. H., Pearson, T. J., et al. 1983, Superluminal Motion in the Quasar 3C 345, ApJ, 271, 536

Venturi, T., Bardelli, S., Morganti, R., & Hunstead, R. W. 1997, Radio Properties of the Shapley Concentration – I. The Abell Cluster A3556, MNRAS, 285, 898

Vermeulen, R. C., Ogle, P. M., Tran, H. D., et al. 1995, When Is BL Lac Not a BL Lac?, ApJ, 452, L5

Walker, R. C., Dhawan, V., Romney, J. D., et al. 2000, VLBA Absorption Imaging of Ionized Gas Associated with the Accretion Disk in NGC 1275, ApJ, 530, 233

Yeom, J. H., Oh, S. J., Roh, D. G., et al. 2009, Development of Software Correlator for KJJVC, JASS, 26, 567